The 8th European Congress on Computational Methods in Applied Sciences and Engineering
ECCOMAS Congress 2022
5-9 June 2022, Oslo, Norway

SIMULATION OF NON-SPHERICAL PARTICLES IN TRIBOLOGICAL THREE-BODY SYSTEMS

Raphael Bilz[1,a] **and Kristin M. de Payrebrune**[1,b]

[1] Institute for Computational Physics in Engineering
Technische Universität Kaiserslautern
Erwin-Schrödinger-Str. 56, 67663 Kaiserslautern, Germany

[a] E-mail: raphael.bilz@mv.uni-kl.de

[b] E-mail: kristin.payrebrune@mv.uni-kl.de

Key words: Hard Particles, Tribological Contacts, Mechanical Process Engineering, Dynamics, Computing Methods

Abstract. Particles between the contact interfaces of two components in relative motion are present in many technical applications and can strongly influence the system behavior. In this context, the focus is often on the investigation of wear and damage. In addition to such undesirable phenomena, however, there is also the targeted use of hard particles, for example in the lapping process. In lapping, hard particles are intentionally inserted between a lapping disc and the workpiece surface to be processed in order to cause material removal with the help of the particles and to improve the morphology of the workpiece surface for certain applications. Many simulations of such tribological systems are based on the assumption of spherical particles. However, both, size and shape of the particles have an essential effect on the system behavior.

Here, an approach is presented in which hard, arbitrarily shaped particles in tribological contacts can be studied a priori using the finite element method by performing indentation simulations for various particle orientations. Based on the results, an orientation-dependent particle model is created for simulations of the overall system, which includes particles in narrow gaps. This modular design allows direct control in the implementation of phenomenological effects and new insights into the behavior of such systems, as well as the estimation of the resulting surface topography.

1 INTRODUCTION

Tribology is a field of science that deals with friction, wear, and related topics such as lubrication [1]. Friction and wear occur at the contact surfaces between two parts moving against each other. In most applications, friction causes reduced mechanical efficiency by converting mechanical energy into thermal energy, and wear limits component life [2]. In contrast, there are machining processes where material removal is intentional, such as grinding or lapping [3, 4].

Both friction and wear depend on many factors, such as the materials and surface geometries of the bodies in contact, the medium between the bodies, the relative motion or the temperature. In tribological three-body systems, there is a non-negligible "third body" between the two "first

bodies" that are in contact. The third body can consist, for example, of gas, liquid, particles, or a mixture thereof, and can significantly affect the system behavior. If the third body includes hard particles, their geometry influences both the system dynamics of the tribological three-body system [5] and the emerging surface topography of the first bodies [6]. Particles can roll in such a system or adhere to one of the two bodies and slide along the other body [1]. The occurring abrasive wear is called two-body abrasive wear if the particles permanently adhere to one of the two bodies, and it is called three-body abrasive wear if the particles temporarily roll and slide [1].

Due to the complexity that tribological systems can exhibit in reality, experiments are currently unavoidable. The modeling and simulation of such systems is usually based on assumptions that are only permissible for certain applications, e.g. the assumption of spherical particles [7]. Furthermore, the dynamics of tribological systems are often not modeled, but only average quantities are determined. In [8], the non-spherical particle geometry is considered using irregular two-dimensional polygons to describe the evolution of the surface topography, but the full three-dimensional particle geometry is not considered. Apart from this, the inertia of the first bodies is not considered in this study. However, especially in tribological three-body systems where non-spherical particles are present, the dynamics of the overall system and that of the particles influence each other. In [9] it is shown that the vertical motion of a first body depends both on the microcontacts and on the global properties of the first body itself. It is also discussed that the interactions between the first bodies are determined by the force-displacement law of the microcontacts. For rolling particles, these force-displacement values change continuously. In addition, the type of load application can decisively influence a tribological system, even if the average load remains unchanged, as shown in [10].

This paper presents a model that accounts for both the changing force-displacement values of rolling particles and, inherently, the type of applied load. Here, weights are used to apply the load. The strong dependence of the tribological overall system on the particles motivates a model that includes both the first bodies and the individual arbitrarily shaped particles. The finite element method can be used to model the forces that occur between the particles and the first bodies during indentation. However, depending on the material behavior and the required accuracy, these simulations are time-consuming, which is why a modular design of the model is pursued. The forces between body and particle are determined a priori for various constellations by finite element simulations. Subsequently, simulations of the tribological overall system can be performed. As demonstrated in the course of this work, the proposed model has remarkable capabilities and properties, such as the determination of non-normally distributed and time-resolved quantities or the estimation of the resulting surface topography.

Section 2 describes the structure of the model with its main attributes and explains the individual submodels in more detail. Section 3 shows simulation results calculated for different parameter combinations using the model described in section 2. Section 4 finalizes with the conclusion.

2 PROCEDURE

This section explains the different submodels of the overall model and the essential elements for building up the simulation model. For the simulation of a tribological system, three modules

representing the three submodels are sequentially run. An overview of the input and output variables of the individual modules can be seen in Figure 1. Module i performs finite element simulations based on the particle shape and material properties of body 1 and body 2 to determine the perpendicular reaction force of the particle as a function of the clearance between the two first bodies. Module ii defines the tribological system and performs simulations based on results obtained from module i. Module iii calculates the topography based on the results of the dynamic simulation from module ii.

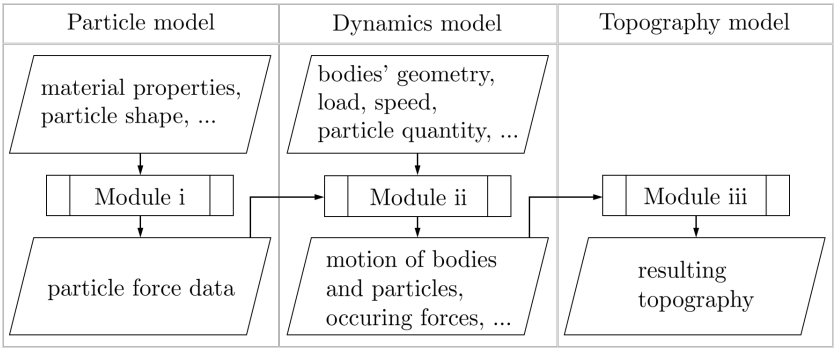

Figure 1: Overview of the proposed model of tribological three-body systems

2.1 Particle model

This subsection is about the creation of the particle force model describing the reaction force F between two bodies in close proximity. Between body 1 made of material 1 and body 2 made of material 2 lies a single rigid particle, as schematically sketched in Figure 2. Neglecting the inertial forces, the forces in both contact surfaces are equal. If the particle shape differs from the spherical shape, the reaction force F_{load} depends on the orientation of the particle located between the bodies. Furthermore, F_{load} depends on the gap height h between the two bodies. In this context, the gap height h describes the distance between the two undeformed surfaces of the bodies. Therefore, for any orientation (α_i, β_i) of the particle, a relation in the form

$$h\left(F_{load}\right) = h_p - \Delta z_1\left(F_{load}\right) - \Delta z_2\left(F_{load}\right) \tag{1}$$

holds. Herein Δz_1 and Δz_2 are the indentation depths into the respective body surfaces and $h_p = h_p\left(\alpha, \beta\right)$ is the orientation-dependent particle height. The orientations are described using the angles α and β, which define the rotation matrix $R^*\left(\alpha, \beta\right) = \left(R_y\left(\alpha\right) \cdot R_x\left(\beta\right)\right)^T$ transforming the original particle geometry to its current orientation (α, β). In order to determine the reaction force F_{load}, some indentation processes are simulated in detail using the finite element method. The orientations under which the particle has a local maximum or minimum height are identified; saddle points are also considered in this procedure. The number of orientations depends, among other things, on the resolution of a particle and the determination method. For the particle shown in Figure 3 (minimum diameter $\min\{h_P\} \approx 2.12\,\mathrm{mm}$, maximum diameter $\max\{h_P\} \approx 4.90\,\mathrm{mm}$), a total of 44 orientations are selected describing local minima, maxima, and saddle points. The 44 orientations are 22 pairs of exactly opposite orientations,

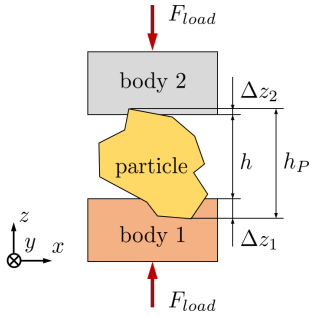

Figure 2: Sketch of particle indentation

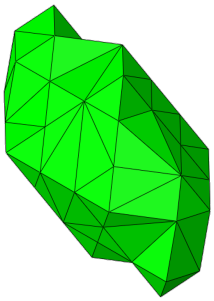

Figure 3: Example particle shape

so that the force-gap height relationship can be easily ascertained for each orientation. For each of the determined orientations, the indentation of the particle into material 1 and 2 are simulated displacement controlled using the finite element analysis program Abaqus/Explicit 2021. Robust simulations for all calculated cases are ensured by including inertial forces and mass scaling. All not strictly monotonic data of the indentation curve are discarded to obtain a bijective relationship. Applying Eq. (1), the particle force F_{load} can be post-processed. Thus, the force-gap height relation is known for all 44 orientations. However, a more general model is needed since arbitrary orientations may occur in the subsequent simulation. Since the angles α and β describe the orientation directions $\vec{r}_i$ very non-uniformly, especially in the region $\beta \approx \pm\frac{\pi}{2}$, for interpolation the orientations (α_i, β_i) are expressed as orientation vectors $\vec{r}_i\,(\alpha_i, \beta_i) = (R^*\,(\alpha_i, \beta_i))^T \cdot \begin{bmatrix} 0 & 0 & 1 \end{bmatrix}^T$ of length 1. If an orientation $\vec{r}^*$ lies between three known orientation vectors $\vec{r}_1$, $\vec{r}_2$ and $\vec{r}_3$, interpolation can be performed. The interpolation weights g_i are calculated based on Delaunay triangulation. For a point within the tetrahedron spanned by $\vec{r}_1$, $\vec{r}_2$, $\vec{r}_3$ and the origin $\begin{bmatrix} 0 & 0 & 0 \end{bmatrix}^T$, the barycentric coordinates b_i can be computed using standardized functions, e.g. the Matlab built-in function `pointLocation`. The vector $\vec{r}^*$ is multiplied by a factor $f < 1$, so that it lies inside the spanned tetrahedron and keeps its direction. Then the interpolation weights $g_i = b_i / \sum_{j=1}^{3} b_j$ are calculated. From the interpolated gap height $h^*\,(F_{load}) = \sum_{i=1}^{3} g_i \cdot h_i\,(F_{load})$, the force F_{load} can be calculated by the inverse of $h^*\,(F_{load})$. This calculation procedure, especially for $F_{load} \to 0$, well approximates the gap height between the support points of the interpolation and consequently the particle shape. At this point, it is advantageous that the orientations (α_i, β_i) of the support points are based on extrema of the particle height $h_p\,(\alpha, \beta)$.

In this work, only the data of the loading curve are further used. In order to take into account the different forces in the loading and unloading case in the subsequent simulation, the previously determined indentation force F_{load} is weighted as a function of the velocities of the two bodies according to the following (highly simplified) rule

$$F = q \cdot F_{load} + (1 - q) \cdot F_{unload} \quad \text{with} \quad q = \frac{1}{2} + \frac{1}{2} \frac{-\left(\dot{z}_2 - \dot{z}_1\right)}{\sqrt{\left(\dot{x}_2 - \dot{x}_1\right)^2 + \left(\dot{y}_2 - \dot{y}_1\right)^2 + \left(\dot{z}_2 - \dot{z}_1\right)^2}}. \tag{2}$$

Assuming ideal plasticity, the unloading force is $F_{unload} = 0$. Factor q results from the relative velocities of the two first bodies. It is $q = 1$ if the two bodies approach each other vertically, $q = \frac{1}{2}$ if the two bodies move only horizontally and $q = 0$ if the two bodies separate vertically.

The possibility of analyzing many different material properties using the finite element method results in a high achievable level of detail of the particle model. The material properties of body 1 and body 2 are summarized in Table 1. Material 1 is made of copper and its material properties are based on a benchmark analysis to be found in the Abaqus Example Guide [11]. Material 2 is 16MnCr5, a low-alloy case-hardened steel with plasticity properties taken from [12].

Table 1: Material parameters of body 1 and 2 [11–14]

	Material 1: Copper			Material 2: Case-hardened 16MnCr5		
General	Density	$\rho = 8970\,\frac{\mathrm{kg}}{\mathrm{m}^3}$	[11]	Density	$\rho = 7760\,\frac{\mathrm{kg}}{\mathrm{m}^3}$	[13]
Elasticity	Linear, isotropic			Linear, isotropic		
	Young's modulus	$E = 110\,\mathrm{GPa}$	[11]	Young's modulus	$E = 210\,\mathrm{GPa}$	[13]
	Poisson's ratio	$\nu = 0.3$	[11]	Poisson's ratio	$\nu = 0.3$	[14]
Plasticity	Perfect plasticity			Johnson-Cook		
	Yield stress	$\sigma_0 = 314\,\mathrm{MPa}$	[11]	Init. yield stress	$A = 588\,\mathrm{MPa}$	[12]
				Hard. coefficient	$B = 680\,\mathrm{MPa}$	[12]
				Hard. exponent	$n = 0.4$	[12]

2.2 Dynamics model

This subsection deals with the dynamics model, which consists of body 1, body 2 and the particles located in between these two bodies. The assembly is shown in Figure 4 on the left. Body 1 is a disc rotating in the plane $z = 0$ and body 2 is a rectangular specimen with dimensions $20\,\mathrm{mm} \times 30\,\mathrm{mm}$ and 30° chamfers at the inlet and outlet with a width of 1.2 mm, as shown in Figure 4 on the right. The axis of rotation of the disc passes the coordinates $(x_c \;\; y_c) = (-0.1 \;\; 0)$, data in SI base units, and the center of the specimen is located in $(x \;\; y) = (0 \;\; 0)$. In this study, multiple instances of the very same particle presented in subsection 2.1 are used. The arrangement of the bodies represents the setup of a tribometer. Body 1 rotates with constant angular velocity ω_L counterclockwise and has no degree of freedom. Body 2 has one degree of

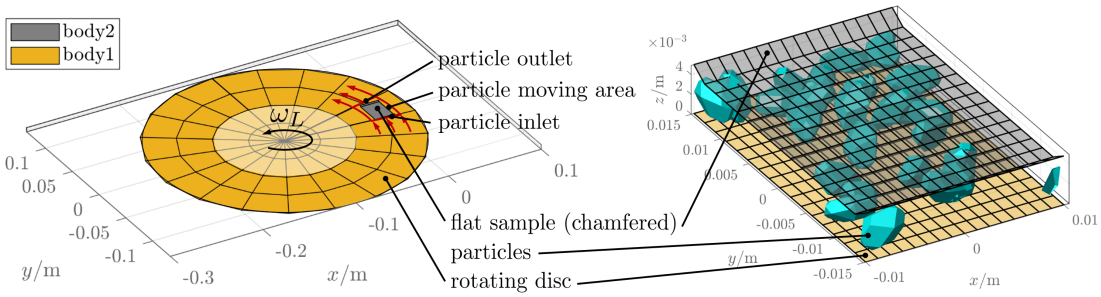

Figure 4: Assembly (left) and detailed simulation area with particles between body 1 and body 2 (right)

freedom of motion and is therewith vertically movable. The gravitational force $F_g = m_2 \cdot g$ acts on body 2 in negative z direction and the occurring particle forces F_k act in positive z direction. The movement of body 2 is given by the equation of motion

$$m_2 \ddot{z}_2 = -F_g + \sum_k F_k. \tag{3}$$

Any load-bearing effect or damping of the system due to a fluid is not yet taken into account.

2.2.1 Particle motion

The following explanations refer to the k-th particle in the dynamic simulation. The particle position is described by the location of the center of gravity (x_k, y_k) in the simulation domain using cartesian coordinates. The angles α_k, β_k resp. γ_k describe the orientation resp. alignment of the particle. Applying rotation matrix $R(\alpha_k, \beta_k, \gamma_k) = R_z(\gamma_k) \cdot (R_y(\alpha_k) \cdot R_x(\beta_k))^T$ and moving the stored particle geometry to its current centroid (x_k, y_k) returns the current particle geometry. The rotation sequence is deliberately chosen so that the angle γ_k has no effect on the particle force F_k, since the force-gap height relationship is invariant with respect to rotation about the vertical axis (assuming isotropic materials). Solely the angles α_k and β_k specify the part of the rotation matrix $R(\alpha_k, \beta_k, \gamma_k)$ which rotates vector $\vec{r}_k = [\cos(\beta_k)\sin(\alpha_k), -\sin(\beta_k), \cos(\alpha_k)\cos(\beta_k)]^T$ in parallel to the z-axis and consequently define the particle orientation for the selection of the corresponding force-gap height curve.

When starting a simulation, a predefined number of particles n_p is generated. In this study, n_p times the same particle is generated. The initial position of the k-th particle is

$$\begin{bmatrix} x_k \\ y_k \end{bmatrix} = r^*(\xi_1) \cdot \begin{bmatrix} \cos(\theta(\xi_2)) \\ \sin(\theta(\xi_2)) \end{bmatrix} + \begin{bmatrix} x_c \\ y_c \end{bmatrix} \tag{4}$$

with $r^*(\xi_1) = \sqrt{\left(r_{\max}^2 - r_{\min}^2\right)\xi_1 + r_{\min}^2}$ and $\theta(\xi_2) = (\theta_{\max} - \theta_{\min})\,\xi_2 + \theta_{\min}$, and the initial particle orientation and alignment $\alpha(\xi_3) = 2\pi\xi_3$, $\beta(\xi_4) = \arccos(2\xi_4 - 1) - \frac{\pi}{2}$, $\gamma(\xi_5) = 2\pi\xi_5$ is defined using uniformly distributed random numbers $\xi_j \in [0, 1]$ for all $\forall j$. As a result, the particles are uniformly oriented, aligned and distributed in the particle moving area of the shape of an annulus sector. The relation $r^*(\xi_1)$ can be obtained using inverse transform sampling [15]. The relations for $\alpha(\xi_3)$ and $\beta(\xi_4)$ are based on explanations in [16].

The velocity of a particle is determined by a linear convex combination of the velocities of body 1 and 2 at the particle position (x_k, y_k).

$$\begin{bmatrix} \dot{x}_k(x_k, y_k) \\ \dot{y}_k(x_k, y_k) \end{bmatrix} = (1 - \lambda) \cdot \begin{bmatrix} \dot{x}_1(x_k, y_k) \\ \dot{y}_1(x_k, y_k) \end{bmatrix} + \lambda \cdot \begin{bmatrix} \dot{x}_2(x_k, y_k) \\ \dot{y}_2(x_k, y_k) \end{bmatrix}. \tag{5}$$

A particle can either stick to body 1 ($\lambda_k = 0$), stick to body 2 ($\lambda_k = 1$), or roll between the two bodies ($\lambda_k = 0.5$). The type of motion λ_k can be defined based on a global or a local criterion. In the context of this paper, $\lambda_k = 0$ holds if the gap height is greater than the particle height, i.e. the particle lies on body 1, and $\lambda_k = 0.5$ holds if the gap height is less than the particle height, i.e. the particle rolls off between body 1 and body 2.

If the particles leave the simulation area, they are reset by the angle $\Delta\theta = \theta_{\max} - \theta_{\min}$ and a new orientation, alignment and radial position are assigned to them based on the random

distributions mentioned earlier. The motion of body 1 transports the particles back into the gap. Particles are temporarily restrained from entering the gap if the current particle height h_k is greater than the current gap height h at the inlet.

The particle orientation during the simulation depends on the contact situation. The angular velocity components ω_{kx} and ω_{ky} are zero if $\lambda_k = 0$ or $\lambda_k = 1$ holds and are approximated by

$$\begin{bmatrix} \omega_{kx} \\ \omega_{ky} \end{bmatrix} = \frac{1}{h} \begin{bmatrix} -\left(v_{2y}\left(x_k, y_k\right) - v_{1y}\left(x_k, y_k\right)\right) \\ v_{2x}\left(x_k, y_k\right) - v_{1x}\left(x_k, y_k\right) \end{bmatrix} \tag{6}$$

using the velocities of bodies 1 and 2 at the particle position (x_k, y_k), if $\lambda_k = 0.5$ holds. The angular velocity component ω_{kz} around the vertical axis equals $\omega_{kz} = (1 - \lambda_k)\ \omega_{1z} + \lambda_k\, \omega_{2z}$. For the calculation of a particle's orientation and alignment, the angular velocity $\vec{\omega}_k$ between two consecutive time steps is assumed to be constant.

2.2.2 Calculation of the dynamics

The Matlab built-in function `ode15s` solves Eq. (3) as a system of first order differential equations

$$\frac{\mathrm{d}}{\mathrm{d}t} \begin{bmatrix} z_2 \\ \dot{z}_2 \end{bmatrix} = \begin{bmatrix} \dot{z}_2 \\ -g + \frac{1}{m_2} \cdot \sum\limits_k F_k \end{bmatrix} \tag{7}$$

for a previously defined time window. After each calculated time step, the particles' positions and orientations are updated. Subsequent to the simulation, individual forces, positions and orientations of all particles as well as the motion of body 2 are available for further investigations.

2.3 Topography model

Currently, the topography formation is computed in a highly simplified manner. Nevertheless, the potential of the proposed modeling of tribological three-body systems can be demonstrated. The change of topography is calculated by subtracting the convex hulls of the penetrating particle shapes with the respective indentation depth from the original body surface, except for already more severely indented areas. Material pile-ups are not considered yet and the original body shape is assumed to be plane for simplicity. For large time steps, the indentation is interpolated between consecutive time steps so that topography changes can be accounted for with desired resolution.

3 RESULTS AND DISCUSSION

This section investigates the capabilities and characteristics of the model presented in section 2. For this purpose, the particle number n_p, tangential velocity v_T at the center of the specimen (body 2) and load F_g acting on the specimen are varied and certain effects on the dynamics and the topography are studied. Since in experiments the load F_g is often applied by adding dead weights, the force F_g is set by specifying the specimen's mass with respect to the gravitational constant $g = 9.81\,\frac{\mathrm{m}}{\mathrm{s}^2}$. Thus, the inertia of the specimen is proportional to F_g. Table 2 shows the parameter combinations of the experimental design. Starting from the central point (test #1) of the experimental plan, one of the three parameters is varied at a time.

Table 2: One-factor-at-a-time experimental design to study impacts of particle number, velocity and load

Test #	1	2	3	4	5	6	7	8	9	10	11	12	13
n_p	30	10	20	40	50	10	10	10	10	10	10	10	10
v_T / $\frac{\mathrm{m}}{\mathrm{s}}$	0.12	0.12	0.12	0.12	0.12	0.04	0.08	0.16	0.20	0.12	0.12	0.12	0.12
F_g / N	300	300	300	300	300	300	300	300	300	100	200	400	500

In the following, the gap height $h_0 = h\,(x = 0, y = 0)$ at the center of the specimen is referred to as the gap height, since the gap height is constant except for the chamfers, whose influence is not studied here. The gap height $h_0(t)$ corresponds to the vertical motion $z_2(t)$ of the flat specimen with the initial gap height $h_0(t = 0) = 3.9\,\mathrm{mm}$ and initial velocity $\dot{h}_0(t = 0) = 0$ for all trials. The distance traveled by the disc underneath the flat sample center is set to $s = 0.5\,\mathrm{m}$. Thus, each particle passes through the gap about 16 to 34 times during a single test, depending on the type of motion λ. Repeated test runs to investigate the effects of the initially randomly distributed particles are omitted due to the likewise randomly distributed reinitialization of the particles after leaving and re-entering the particle moving area.

3.1 Dynamics investigation

Figure 5 shows the time histories of the sum of the particle forces, individual particle forces, number of loaded particles, gap height h_0, and gap height velocity $\dot{h}$ for test #1. The total normal force F_N, which is identical to the sum of the particle forces, shows strong fluctuations and occasionally high peaks. However, the individual particle loads are much lower. Normal force peaks are distributed among multiple particles, so the number of active particles changes frequently. Nevertheless, the non-spherical shape of the rolling particles on the one hand and the alternation of the particles in contact on the other hand causes a varying gap height h_0. Like h_0, the gap height velocity $\dot{h}_0$ remains in a uniform range except for a few exceptions.

The distributions of total normal force F_N, gap height h_0, and gap height velocity $\dot{h}_0$ vary, sometimes significantly, when particle number n_p, tangential velocity v_T, and weight force F_g change. In Figure 6, the means of these variables are indicated by a black circle, and the minima and maxima are indicated by error bars with estimated probability density functions attached. In the plots of the total particle force F_N, the maxima are outside the plotted range. In all cases, the maximum values reach several thousand Newtons and are highly scattered. Therefore, the force range shown is intentionally chosen to appropriately represent the distributions. As expected, the mean values of $\dot{h}_0$ are about zero, because the flat sample moves neither up nor down in the long run. Also the mean value of the total normal force F_N corresponds to the set weight F_g.

When increasing the particle number n_p, the entire distribution of the gap height h_0 shifts upward, because the load can be distributed over more particles, so that the indentation depths tend to decrease. No effect is detected with certainty for the two output variables $\dot{h}_0$ and F_N.

The velocity v_T shows clear effects on all three quantities investigated. The maximum and mean value of h_0 increases with increasing velocity v_T, since the flat specimen temporarily loses contact with the particles due to high vertical accelerations. That also manifests in a two-sided

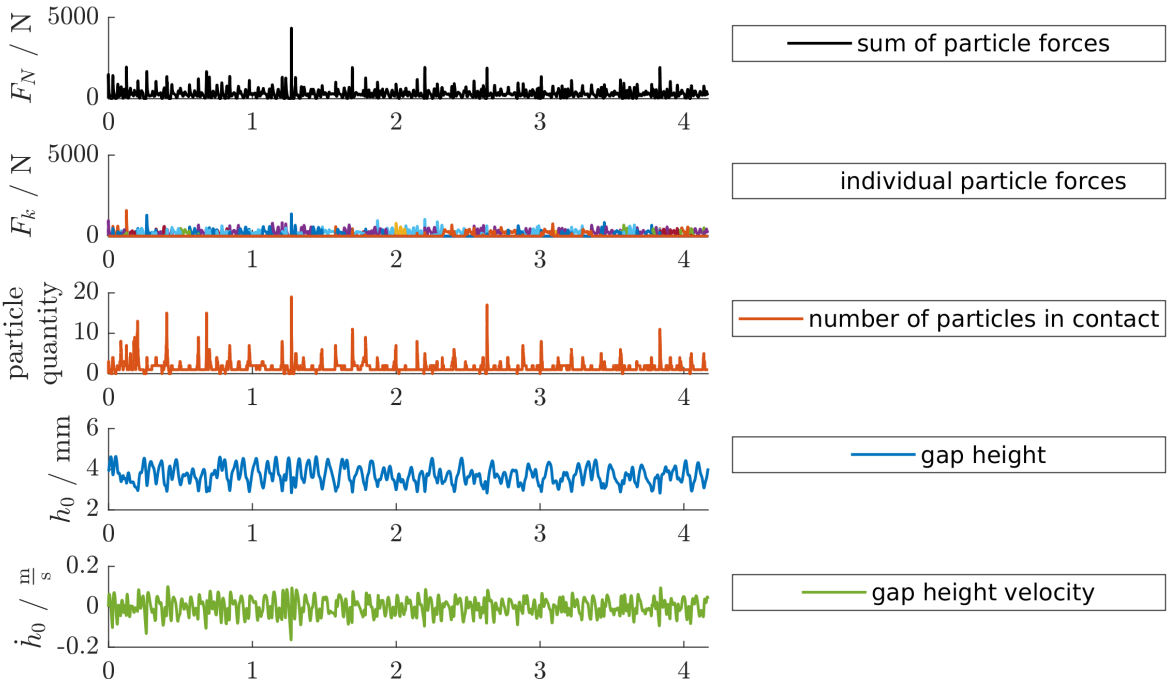

Figure 5: Time history of sum of particle forces (row 1), individual particle forces (row 2), number of loaded particles (row 3), gap height (row 4), and gap height velocity (row 5) for test #1

broadening of the $\dot{h}_0$ distribution. The specimen moves upward when it contacts a rolling particle that is rising. The faster the particles roll, the broader the distribution of the vertical velocities $\dot{h}_0$ (within the parameter range tested). F_N is very tightly distributed around the mean value for the smallest tested velocity v_T. The distribution widens with increasing velocity and finally consists of few widely scattered very high forces and numerous very low forces $F_N \approx 0$, where the specimen loses contact. This phenomenon we already discussed in [5].

The load F_g also has a significant effect. The entire range of gap heights shifts when F_g is increased. Minimum, mean as well as maximum gap height show a decreasing trend. The $\dot{h}_0$ distribution slightly tightens from $F_g = 100\,\mathrm{N}$ to $F_g = 500\,\mathrm{N}$, possibly due to the increased inertia of the specimen caused by the increase in F_g. For high F_g, the middle percentiles of the occurring normal forces are relatively symmetrically distributed. For low forces, the distribution of F_N is skewed similarly to the force distributions for high velocities v_T. Given a constant load, spiky particle segments tend to penetrate deeper into the surface than flat ones. Thus the contribution of the non-round particle shape to the vertical motion h_0 of the specimen decreases at higher loads. The impact of load induced deformation on the velocity dependence mentioned before is also discussed in [5] and quite expected to occur for sufficiently high velocities v_T.

All in all, the model reproduces physically consistent results. The mean gap height velocity $\dot{h}_0$ is almost zero and the mean force F_N is equal to F_g. Also phenomena known from literature concerning the velocity dependence are at least qualitatively met in this first evaluation. It remains open to what extent this type of modeling can reproduce tribological three-body systems under real test conditions, and to what extent individual parts of the model need to be refined.

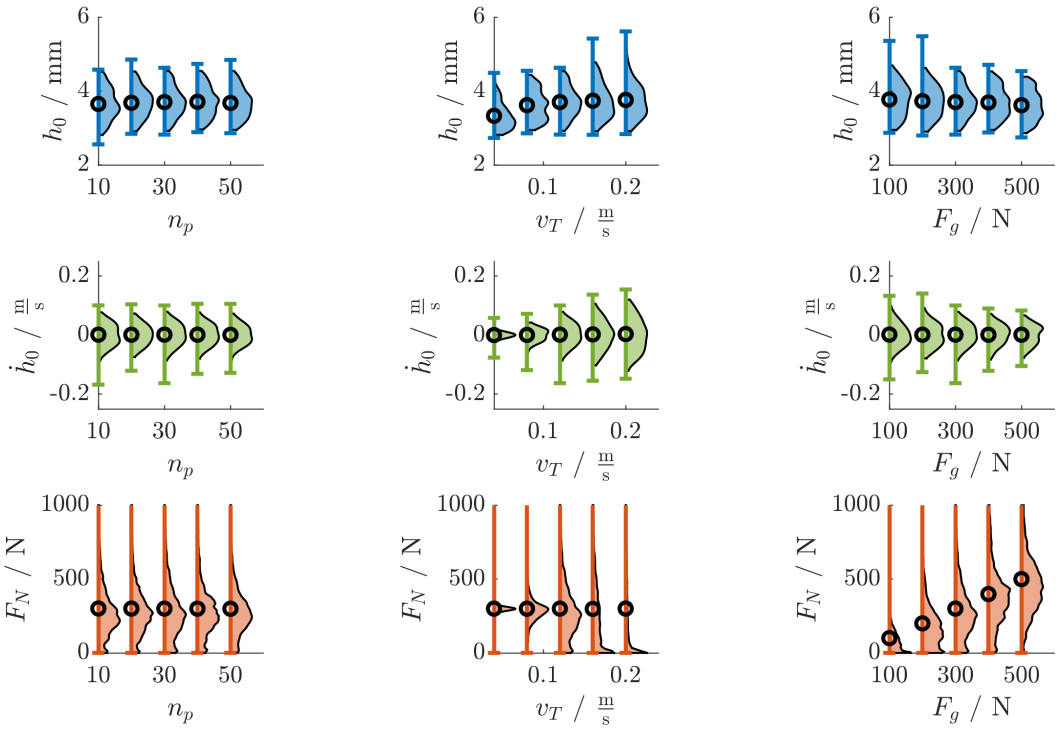

Figure 6: Occurring gap heights h_0 (top), gap height velocities $\dot{h}_0$ (middle) and normal forces F_N (bottom) are shown as a distribution for $v_T = 0.12\,\frac{\mathrm{m}}{\mathrm{s}}$, $F_g = 300\,\mathrm{N}$ over n_p in column 1, for $n_p = 30$, $F_g = 300\,\mathrm{N}$ over v_T in column 2 and for $n_p = 30$, $v_T = 0.3\,\frac{\mathrm{m}}{\mathrm{s}}$ over F_g in column 3

3.2 Topography investigation

In order not to exceed the scope of the publication, the topography is only briefly touched upon here. Figure 7 shows the resulting topographies for tests #2, #1, and #5 with particle numbers 10, 30, and 50. The color scale on the right applies equally to all three plots and ranges from yellow (no indentation) to blue (high indentation depth). Here, the chamfer is neglected when calculating the topography change $\Delta z_2(x, y)$. All locations with non-zero Δz_2 values contribute to the processed area A_{pro}. Table 3 shows the maximum values of Δz_2 and the fraction of the processed area A_{pro} relative to the total area A_{tot} for different n_p. Without test repetitions, the variance of these results cannot be quantified. Nevertheless, the results reveal quite realistic trends. The maximum indentation depth decreases and the processed area increases degressively with increasing particle number.

Table 3: Impact of particle number n_p on max. of indentation depth Δz_2 and processed area fraction $\frac{A_{\mathrm{pro}}}{A_{\mathrm{tot}}}$

n_p	10 (Test #2)	30 (Test #1)	50 (Test #5)
$\max\{\Delta z_2\}$	364.2 µm	281.5 µm	206.7 µm
$\frac{A_{\mathrm{pro}}}{A_{\mathrm{tot}}}$	15.3 %	19.8 %	20.1 %

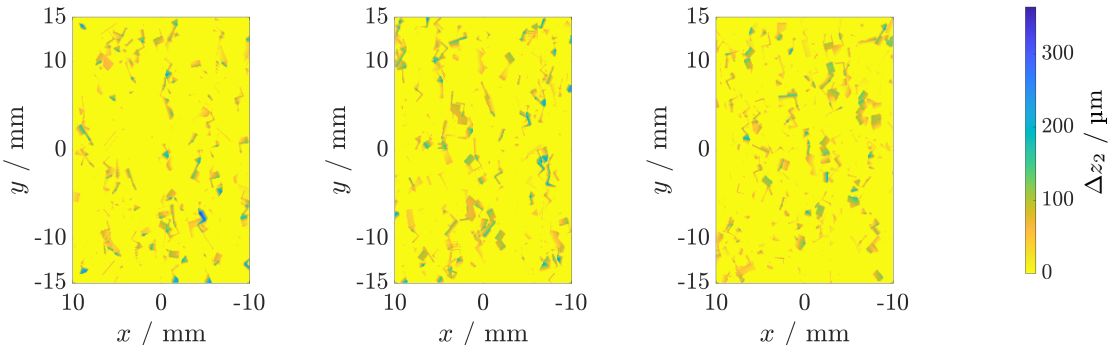

Figure 7: Resulting topography of the specimen for particle numbers 10 (left), 30 (mid), and 50 (right)

4 CONCLUSION

This publication presents a mostly deterministic model of tribological three-body systems. The subdivision of the overall model into three decoupled modules provides both the possibility to enhance them for specific applications and to achieve better performance than fully coupled simulations. The model structure is particularly designed to account for non-spherical particle shapes. All material models available in finite element programs can be used in the particle model. Independently, the dynamics model controls motion and constraints of the first bodies as well as the situation-dependent behavior of the particles, e.g. rolling or sliding. Parameters that cannot be adjusted economically in experiments, such as initial particle positions and orientations, are randomly generated in the model. Finally, the locally resolved loading history along the body surfaces enables subsequent analyses and the calculation of the resulting topography.

A one-factor-at-a-time experimental design is used to investigate the effect of particle number, tangential velocity, and applied load on a simple tribological three-body system. The obtained results are consistent and the input parameters show reasonable effects. A major advantage of this modeling type is that the results of dynamic simulations are *time-resolved*. Even local quantities such as individual particle loads and indentation depths are accessible output variables. Not only mean values can be calculated, but the entire *probability distribution* of the values that occur can be estimated. The mean value often has insufficient meaning for reliable predictions, e.g. if a material-specific strength is temporarily exceeded. In contrast, distributions allow estimating whether and how often a limit is exceeded. For example, the normal force distribution shows a clear increase in skewness with increasing velocity within the parameter range investigated, while the mean value remains constant.

The model currently represents some phenomena in a very simplified way. However, the possibilities to incorporate and investigate problem-specific phenomena are almost unlimited. In the future, the model could be used to optimize operating parameters or selected response variables while complying with certain constraints, e.g. maximum particle loading.

ACKNOWLEDGEMENTS

The present publication was funded by the Deutsche Forschungsgemeinschaft (DFG, German Research Foundation) – Project-ID 172116086 – SFB 926.

REFERENCES

[1] G. W. Stachowiak, *Engineering Tribology*. Oxford: Elsevier, 2014.

[2] M. Woldman, *An experimental and theoretical investigation into three-body abrasive wear*. PhD thesis, University of Twente, 2014.

[3] F. Klocke, *Fertigungsverfahren 2*. Springer-Verlag GmbH, 2017.

[4] I. Marinescu, E. Uhlmann, and T. Doi, *Handbook of Lapping and Polishing*. CRC Press, 2007.

[5] R. Bilz and K. M. de Payrebrune, "Investigation of the influence of velocity in a tribological three-body system containing a single layer of rolling hard particles from a mechanical point of view," *Tribology International*, p. 106948, 2021.

[6] G. Stachowiak and G. Stachowiak, "The effects of particle characteristics on three-body abrasive wear," *Wear*, vol. 249, pp. 201–207, may 2001.

[7] M. Khonsari, "On the modeling of multi-body interaction problems in tribology," *Wear*, vol. 207, pp. 55–62, jun 1997.

[8] U. Heisel and J. Avroutine, "Process analysis for the evaluation of the surface formation and removal rate in lapping," *CIRP Annals*, vol. 50, no. 1, pp. 229–232, 2001.

[9] V. Popov and S. Psakhie, "Numerical simulation methods in tribology," *Tribology International*, vol. 40, pp. 916–923, jun 2007.

[10] R. Bilz, P. Sridhar, and K. M. de Payrebrune, "Parameter identification aspects of tribological systems containing hard particles," *PAMM*, vol. 21, dec 2021.

[11] Dassault Systèmes S.A., "Impact of a copper rod." `https://help.3ds.com/2021/English/DSSIMULIA_Established/SIMACAEBMKRefMap/simabmk-c-rodimpact.htm?contextscope=all&id=1f8865ac390d43dea6699f1b0dc71b0f`. Accessed: 2022-05-31.

[12] G. Szabó and J. Kundrák, "Numerical research of the plastic strain in hard turning in case of orthogonal cutting," *Key Engineering Materials*, vol. 496, pp. 162–167, dec 2011.

[13] Deutsche Edelstahlwerke GmbH, "Werkstoffdatenblatt carbodur 7131 / 7139." `https://www.dew-stahl.com/fileadmin/files/dew-stahl.com/documents/Publikationen/Werkstoffdatenblaetter/Baustahl/1.7131_1.7139_de.pdf`. Accessed: 2022-05-31.

[14] V. Läpple, *Einführung in die Festigkeitslehre*. Vieweg+Teubner Verlag, 2011.

[15] K.-H. Waldmann and W. E. Helm, *Simulation stochastischer Systeme*. Springer Berlin Heidelberg, 2016.

[16] E. W. Weisstein, "Sphere point picking." `https://mathworld.wolfram.com/SpherePointPicking.html`. Accessed: 2022-05-31.